PAPER

Check for updates

Structural basis of a 2-oxoglutarate-dependent heme-oxygenase-like enzyme HamA in fragin biosynthesis

Binbin Su, [ID] [a] Tongtong Zhang, [ID] [b] Yang Yu [ID] *[a] and Haiping Liu [ID] *[c]

The fungicide fragin, which contains a diazeniumdiolate moiety, exhibits a broad spectrum of biological activities. HamA, the key enzyme responsible for forming the nitrogen–nitrogen bond in this moiety, was investigated in this study. We determined the crystal structure of HamA at 2.0 Å resolution, revealing a mononuclear iron center in the active site coordinated by both the "2His–1Glu" motif and an acetate group. Notably, HamA adopts a heme oxygenase-like fold, forming a hydrophobic cavity within a helical bundle that likely accommodates the substrate. Structural data confirmed the presence of an acetate and a formate group near the active site and microscale thermophoresis (MST) experiments further demonstrated HamA's ability to bind 2-oxoglutarate (2OG) with a dissociation constant (K_d) of 208 ± 1.42 μM. In summary, this study elucidates the 2OG-dependent heme-oxygenase-like enzyme HamA with a monoiron active center, providing critical structural insights into the mechanistic formation of the diazeniumdiolate moiety in fragin.

Introduction

Heme oxygenases typically use heme as a substrate or cofactor to catalyze the oxygenative cleavage of the α-methine bridge of the heme porphyrin ring, producing non-toxic biliverdin, the gaseous signalling molecule carbon monoxide (CO), and free iron.[1–3] This process confers physiological functions such as anti-inflammatory, antioxidant, and anti-apoptotic effects. Heme oxygenases exhibit a characteristic conserved 7-α-helical structure that encapsulates the heme cofactor.[4,5] However, this multi-α-helical structure is also found in enzymes that are not involved in heme degradation or even do not require metal cofactors for catalysis. For example, AetD catalyzes the oxidative rearrangement of brominated tryptophan to a nitrile in the biosynthesis of aetokthonotoxin, while TenA participates in the salvage pathway of thiamine (vitamin B_1), catalyzing the recycling of thiamine degradation products.[6–8]

The natural product fragin, a member of the diazeniumdiolate family exhibits significant pharmaceutical potential due to its antifungal, antibacterial, antiviral, and antitumor activities.[9–12] Its biosynthetic gene cluster was identified from *Burkholderia cenocepacia* H111, which is composed of *HamA–F*.[13] The initial substrate valine is tethered to the non-ribosomal peptide synthetase HamD to start the N–N bond formation. In this progress, HamA and HamC were thought to play critical roles. HamC was reported to be a tailoring enzyme that oxygenates the α-amine of L-valine tethered to the thiolation domain (T, *apo*T) of the NRPS-like enzyme HamD.[14,15] It converts the valine amine to a hydroxyl-amine (+16 Da) intermediate (HamC–*holo*T-valine) *via* two-electron oxidations.[16] HamA was predicted to be a heme-oxygenase-like enzyme based on sequence similarity. However, the structure, catalytic activity and the role for fragin synthesis of HamA remain unknown.[13] Due to the intriguing chemical reactions it catalyzes and its key roles in the biosynthesis of important natural products, HamA is of great interest for structural and mechanistic studies.

Here, we aim to elucidate the mechanism of HamA through structural and functional studies. Our X-ray crystal structure and inductively coupled plasma mass spectrometry (ICP-MS) results established that HamA utilizes a mononuclear iron and 2-oxoglutarate as cofactors, a feature unique among characterized heme oxygenase-like domain-containing oxidases (HDOs) to date. Nano-scale liquid chromatography coupled with ultra-high resolution mass spectrometer (LC-HRMS) revealed that HamA is a 2-oxoglutarate-dependent mono-oxygenase capable of incorporating an oxygen atom into its substrate, HamD–T-valine.

[a]Institute of Biochemical Engineering, Key Laboratory of Medical Molecule Science and Pharmaceutics Engineering of Ministry of Industry and Information Technology, School of Chemistry and Chemical Engineering, Beijing Institute of Technology, China. E-mail: yang_yu@outlook.com

[b]Tianjin Institute of Industrial Biotechnology, Chinese Academy of Sciences, China. E-mail: zhang_tt@tib.cas.cn

[c]Division of Life Sciences and Medicine, University of Science and Technology of China, Hefei, Anhui, China. E-mail: haipingliu@ustc.edu.cn

Materials and methods

Protein expression and purification

The HamA gene was cloned into pET22b and transformed into *E. coli* BL21(DE3). A single colony was inoculated into 10 mL LB medium containing ampicillin and grown overnight, then diluted 1 : 100 until reaching an OD_{600} of 0.6–0.8. Protein expression was induced with 0.5 mM IPTG at 16 °C for 16 h. Cells were harvested by centrifugation (4000 rpm, 30 min), resuspended in lysis buffer (20 mM Tris–HCl pH 8.0, 200 mM NaCl; 10 mL per g pellet), and lysed by sonication. After centrifugation (16 000 rpm, 30 min, 4 °C), the supernatant was loaded onto a Ni^{2+}-charged Chelating Sepharose Fast Flow column (GE Healthcare) pre-equilibrated with lysis buffer. The protein was eluted with a stepwise imidazole gradient (20–500 mM) in lysis buffer, with the target eluting at 200 mM imidazole. Further purification was performed by size-exclusion chromatography (Superdex 200 10/300 GL, GE Healthcare) in 20 mM Tris–HCl pH 8.0, 200 mM NaCl. Target fractions were pooled, concentrated to 10 mg mL^{-1}, and their purity was assessed by SDS-PAGE before crystallization trials.

Crystallization and data collection

Crystallization screening was performed at 16 °C using Hampton Research kits (Crystal Screen, Crystal Screen 2, Index, and PEGRx 1,2) with the sitting-drop vapor-diffusion method. Conditions were optimized *via* hanging-drop vapor diffusion. X-ray diffraction data were collected at 100 K (cooled by liquid nitrogen) on a Rigaku MicroMax-007HF generator equipped with an Rigaku HyPix-Arc 150 detector ($\lambda = 1.54$ Å), without additional cryo-buffer. Each image was collected with an oscillation angle of 0.5 and an exposure time of 30 s. The distance from crystal to the detector was set to 60 mm. Diffraction images were processed using CrysAlisPro for indexing, integration, and scaling.[17]

Structure determination and refinement

The structure was solved by Molecular Replacement using Phaser program in the CCP4 suite using the predicted structure of HamA from Alphafold3 as the search model.[18–21] REFMAC5 was used for refinement, Coot was used for model building and structural figures were prepared by using PyMOL.[22–24]

UV-vis to assess diiron center

Absorption spectrum of 100 μM of either HamA or a diferric azoxy synthase VlmB were recorded using a MAPADA UV3100 spectrometer. Both proteins were recorded with a detection range of 300–800 nm and a scanning interval of 1 nm.

Metal content analysis by inductively coupled plasma-mass spectrometry (ICP-MS)

A sample of 100 nmols HamA was diluted in 10 mL of 10% nitric acid and incubated at 200 °C for 2 hours until the digestate volume was reduced to 1 mL. The digest was then diluted with Ultra Trace Elemental Analysis Grade water to a final volume of 10 mL. Amount of iron ion in the HamA digest was analyzed by Inductively Coupled Plasma Mass Spectrometry (ICP-MS) on a Agilent 5800 spectrometer, calibrated by standard solutions from Sigma.

Molecular docking

Molecular docking of HamA with 2OG was performed using ChemDraw 2019 and Autodock 4.0 (The Scripps Research Institute).[25,26] The regularized protein served to identify key amino acids in the predicted binding pocket. Autodock performed interactive docking of all 2OG conformers to the selected active site following energy minimization. A binding energy was assigned to the docked 2OG according to its binding mode on the binding site. Semi-flexible docking was performed with protein rigid and ligand flexible, using Induced Fit method and London dG scoring for 20 runs, with the top-ranked conformation selected for analysis.

Microscale thermophoresis

The equilibrium dissociation constants (K_d) were determined using a Monolith NT.LabelFree instrument (NanoTemper Technologies).[27] HamA (2 μM) was incubated with 2OG (0.6 μM to 20 mM) for 10 min in running buffer (20 mM Tris–HCl, 200 mM NaCl, pH 8.0). The samples were loaded into the NanoTemper glass capillaries and microthermophoresis was carried out using 80% light emitting diode power and 80% MST. The K_d values were calculated using the MO.Affinity Analysis software from duplicate reads of measurements.

Modification of either *holo*T-Val or HamC–*holo*T-Val by HamA

The *holo*T-Val and HamC–*holo*T-Val loading procedures were performed using the same method as described in the previous assay (SI Methods 1.2 and 1.3, Fig. S1).[15] HamA (20 μM) was pre-incubated with 40 μM ferrous ammonium sulfate and 1 mM sodium ascorbate in 25 mM phosphate buffer (pH 7.4) for 20 min on ice. An equal volume of this mixture was added to the *holo*T-valine or HamC–*holo*T-valine reaction and incubated for additional 1 h at room temperature. Finally, the sample was diluted to 10 μM *apo*T with water for LC-HRMS analysis.

LC-HRMS analysis of HamA reactions toward T-domain protein substrates

The samples from *holo*T-valine with HamA reaction solution were desalted with ZipTip (C4, 1000 Å, Merck) before analyzed by Vanquish Neo system (Thermo) followed by tandem MS, a Thermo Fisher Orbitrap Eclipse spectrometer. Samples were separated on a homemade C4 (1000 Å) 100 mm × 100 μm column with the flow rate of 600 μL min^{-1}. Solvent A consisted of 0.1% (v/v) formic acid in water, and solvent B consisted of 0.1% (v/v) formic acid in 80% (v/v) acetonitrile. The samples were eluted by 20% B for 2 minutes, followed by a linear gradient of 20–85% B over 15 minutes, 85–100% B over 1 minute, maintained 100% B over 5 minutes, 100–20% for 1 min and keep 20% B for another 1 minute. The mass spectrometer worked under positive ion mode using the following nanoESI

source parameters: spray voltage 2200 V, Ion transfer tube temperature 320 °C, RF 40%. The full scan acquisition was performed with MS1 resolution of 240 000, the full scan range is between 500 and 2000 m/z with max injection time of 50 ms under AGC 4×10^5.

Results and discussion

Overall structure of HamA

Single crystals grew in a solution containing 0.1 M sodium acetate trihydrate pH 5.0, 2.85 M sodium formate and 5% (v/v) glycerol. The crystal structure of HamA was determined and refined to a resolution of 2.0 Å. The final model exhibits good geometry, with R-factor/R_{free} values of 0.170/0.219 (Table 1). The crystal belongs to the space group $P42_12$, with one HamA monomer in the asymmetric unit. The overall structure consists of nine α-helices, seven of which form a super helical domain bundle, displaying a structural conformation consistent with heme dioxygenases-like enzymes (Fig. 1).[28,29] Among these, α-helices 1, 2, 3, and 4 are the four primary α-helical bundles that traverse the HamA structure, accompanied by three auxiliary α-helical bundles, which enhance the stability of the core
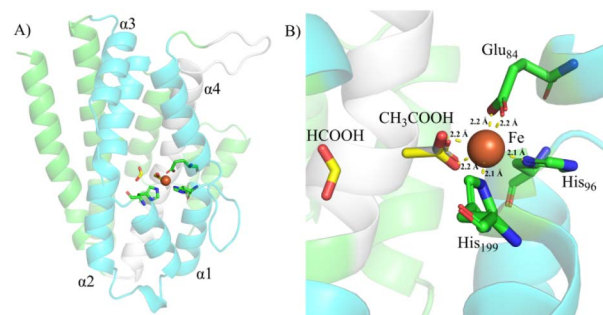

Fig. 1 (A) Overall structure and (B) active center of HamA (PDB ID 9VWB).

structure. This also closely resembles the unique conserved 4-α-helical bundle structure found in iron storage proteins.[30]

The free R factor was calculated using 5% of reflections omitted from the refinement.

A single metal binding site was observed in the electron density map. Inductively coupled plasma mass spectrometry (ICP-MS) confirmed the presence of iron ion, and the metal analysis revealed a stoichiometric ratio of Fe : protein (1.5 : 1, Table S1), consistent with the mononuclear iron center observed in the structural data. Furthermore, the UV-visible absorption spectroscopy of the purified HamA lacks a peak at 360 nm (Fig. 2), a typical spectral characteristic of diferric centers further corroborating that HamA has a mono iron center.

Putative binding of 2-oxoglutarate

In the iron center of the crystal structure, additional electron density can be modeled as a formate and an acetate molecule, possibly from the crystallization solutions (Fig. 3). Residues Glu184 and His96 located in the α1 helix and His199, and Glu84 situated in the α3 helix of the 4-α-helical bundle, coordinate with the iron center in a tetrahedral arrangement, while the remaining two coordination sites are occupied by the carboxyl group of acetate. The structural features resemble the facial triad motif (2His–1Glu/Asp) observed in non-heme iron-2OG-dependent enzymes but exhibit a unique "meridional" structural characteristic. Interestingly, a clearly visible electron

Table 1 Crystallographic parameters of HamA

Diffraction data	
Space group	$P42_12$
Cell dimensions	
a, b, c (Å)	101.6, 101.6, 46.9
α, β, γ (°)	90, 90, 90
Resolution range (Å)	28.5–2.00(2.08–2.00)
Number of unique reflections	16 979
Data completeness (%)	99.2(96.6)
Redundancy	11.7 (10.9)
$I/\sigma(I)$	12.1(5.5)
$R_{pim}{}^a$	0.072(0.417)
Refinement	
R-factor/$R_{free}{}^b$	0.170(0.219)
r.m.s.d. bond length (Å)	0.008
r.m.s.d. bond angles (°)	1.425
Mean B factor (Å^2)	
Protein main-chain atoms	19.528
Protein side-chain atoms	23.762
Water molecules	25.746
Fe	15.140
Na	30.730
Number of atoms	
Protein	1977
Water molecules	144
Fe	1
Na	1
Ramachandran plot statistics	
In preferred regions (%)	98.34
In allowed regions (%)	1.66
Outliers (%)	0.00

^{a} R_{pim} (precision-indicating R) = sum(sqrt(1/(N − 1))(|Ihl − $\langle Ih \rangle$|))/sum($\langle Ih \rangle$). ^{b} R-factor = $\sum \|F_{obs}| - |F_{calc}\|/\sum |F_{obs}|$, where F_{obs} and F_{calc} are observed and calculated structure factors.
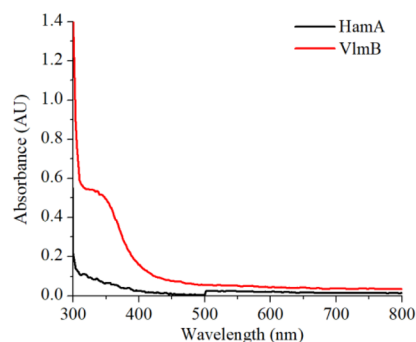
Fig. 2 UV-visible absorption spectrum of HamA and a diferric azoxy synthase VlmB.[31]

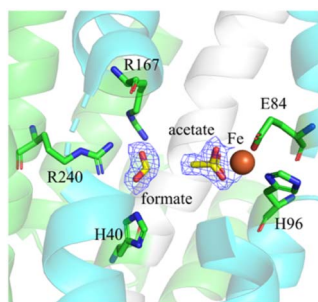© 2025 The Author(s). Published by the Royal Society of Chemistry

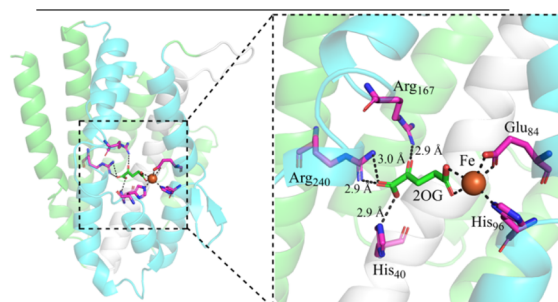Fig. 3 Electron density of formic acid and acetic acid at the active center of HamA.

Fig. 4 Results of the molecular docking analysis between HamA and 2OG.

density corresponding to a formate molecule is observed at a distance of 3.8 Å from the coordinated acetate. Together, the formate and acetate molecules resemble 2OG.

As is typical for 2OG oxygenases, 2OG serves as an essential co-substrate that coordinates the mononuclear iron center in the active site, facilitating both structural integrity and oxygen activation. This binding is a prerequisite for oxygen activation and subsequent substrate oxidation. Despite extensive co-crystallization trials with 2OG, no diffraction-quality crystals of the complex were obtained. Therefore, we performed molecular docking between HamA and 2OG using Autodock software, and the results are shown in Table 2. The top-ranked conformation from the docking simulation exhibited the most favorable estimated free energy of binding (-9.62 kcal mol^{-1}), indicating a strong potential for 2OG to bind within the active pocket of HamA. This result was selected from multiple independent runs based on its superior energetic profile and cluster membership. The conformation underwent further local energy refinement, resulting in a final intermolecular energy that reflects the stability of the optimized complex. These results collectively demonstrate that the active pocket of HamA can stably accommodate the 2OG molecule. The docking results corresponding to the top-ranked molecular conformation were further visualized, as shown in Fig. 4.

2OG occupies the central cavity of HamA, engaging in crucial interactions with three key residues: His40, Arg167, and Arg240. Specifically, its γ-carboxyl group coordinates with the Fe ion in

the active center, while the α-carboxyl moiety participates in multiple interactions – forming a salt bridge between its carbonyl oxygen and the guanidinium group of Arg240. Its hydroxyl oxygen establishes a 2.9 Å hydrogen bond with the N^{ε} of His40, with the ketone oxygen simultaneously forming another 2.9 Å hydrogen bond with the guanidinium group of Arg167. Molecular docking results further confirm that six key residues (H40, E84, H96, H199, R240, and R167) are essential for 2OG binding.

To test this hypothesis, we investigated the binding ability of HamA to 2OG using Microscale Thermophoresis. The results demonstrated that HamA can effectively bind to 2OG, and the binding affinity exhibited varying response amplitudes at different concentrations of 2OG, consistent with a single-site binding model. By plotting the binding curve with the logarithm of protein concentration on the X-axis and ΔF_{norm} on the Y-axis, as shown in Fig. 5, the dissociation equilibrium constant (K_d) of HamA for 2OG was determined to be 208 ± 1.42 μM.

Activity of HamA

To characterize the activity of HamA, we sought to reconstitute its activity *in vitro*. However, HamA did not modify free valine. Therefore, we propose that the amino group of L-valine tethered to the thiolation domain of the nonribosomal peptide synthetase-like HamD, could be oxidized to a hydroxylated product by HamA. To investigate this hypothesis, we performed molecular docking of HamA with PPant-bound valine. The

Table 2 The binding energy of molecular docking between HamA and 2OG

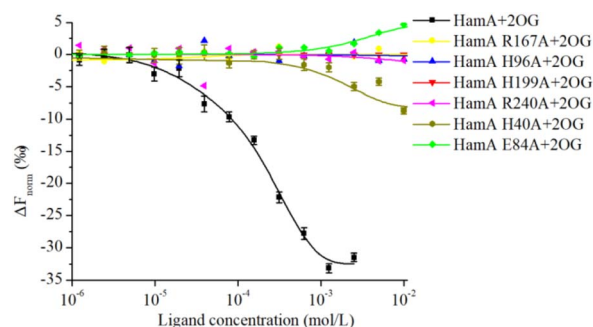| Rank	Binding energy (kcal mol^{-1})
1	-9.62
2	-7.65
3	-7.11
4	-7.93
5	-4.37
6	-3.12
7	-5.65
8	-1.97
9	-4.79
10	-4.93

Fig. 5 The binding ability of HamA to 2OG using Microscale Thermophoresis.
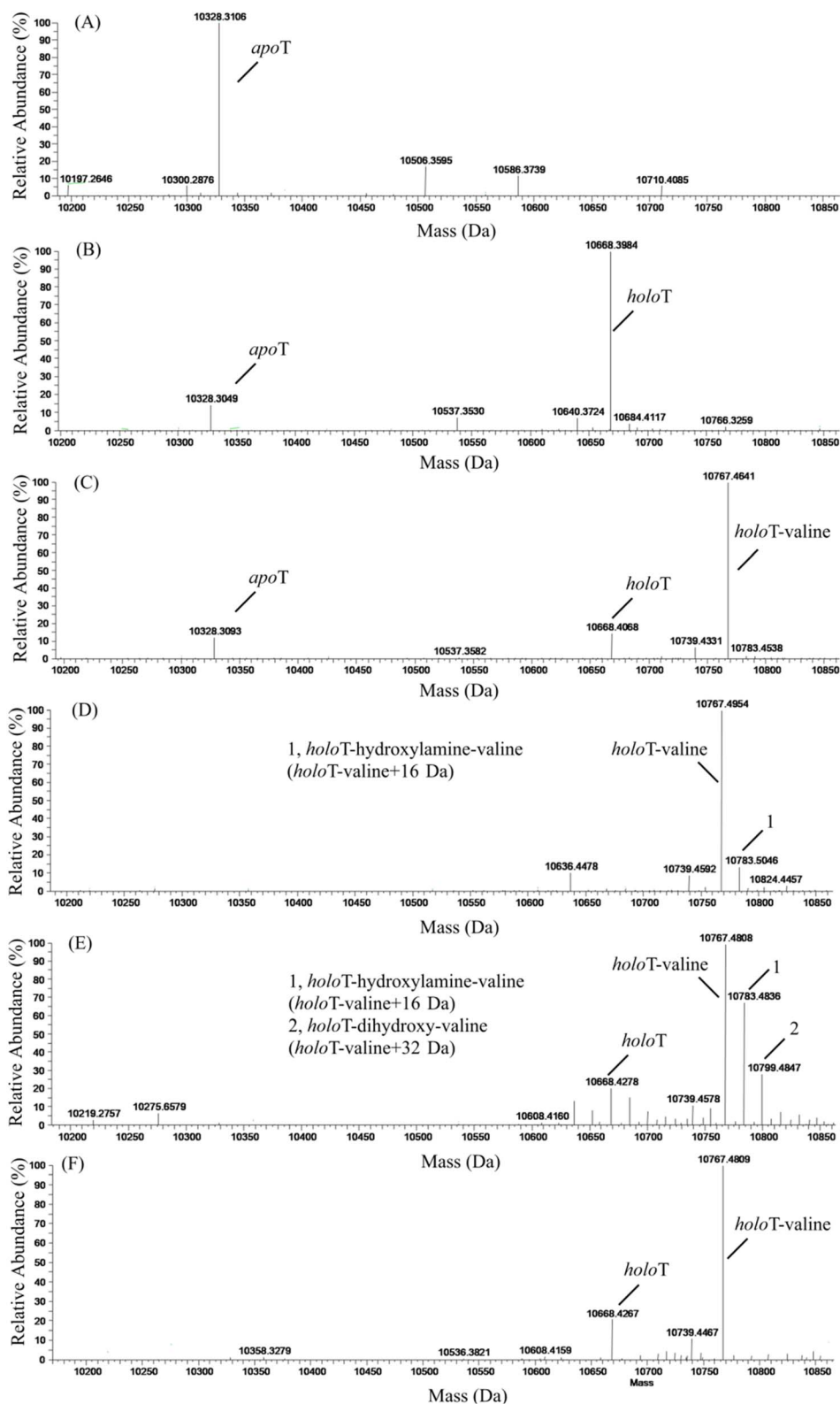
Fig. 6 Deconvoluted mass spectra of (A) *apo*T, (B) *holo*T, (C) *holo*T-valine, (D) modification of *holo*T-valine by HamC, (E) *holo*T-dihydroxy-valine generated by HamA, and (F) reaction with HamA R240A mutant showing no product formation.

docking results revealed that PPant-bound valine fits well into the iron active site, where it coordinates to the metal center together with the residues His40, His96, and Glu84 (Fig. S2). To

experimentally validate the binding, we expressed and purified the thiolation domain of HamD as a truncated protein (HamD–T, *apo*T, Fig. 6A). PPant-bound HamD–T (*holo*T, Fig. 6B) was
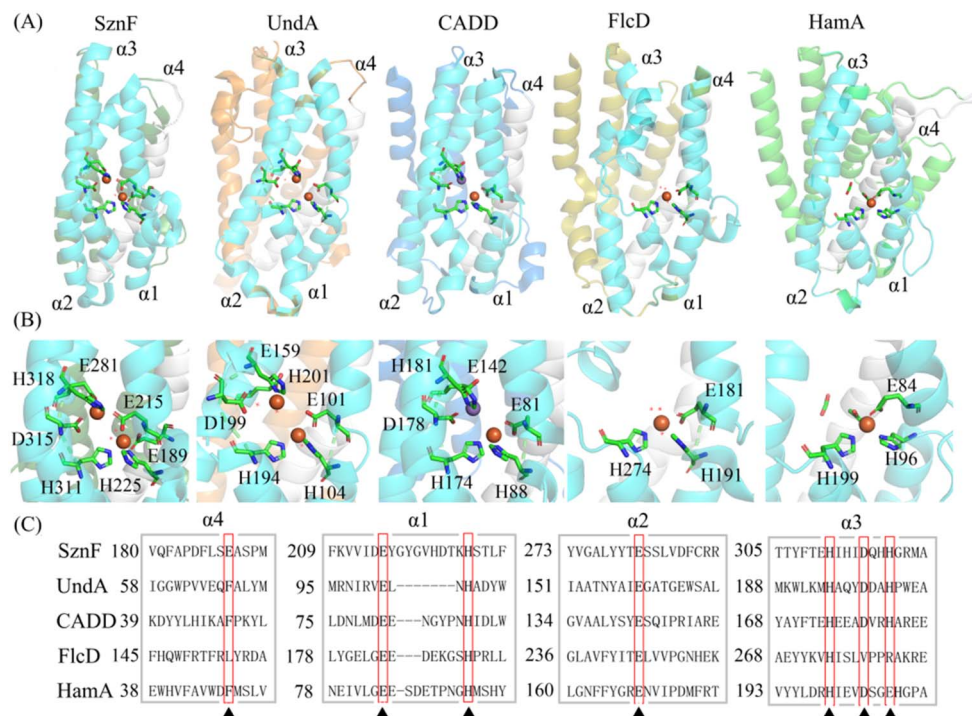
Fig. 7 Structural comparison and sequence alignment of HamA and functionally diverse HDO proteins. SznF (PDB ID 6XCV), UndA (PDB ID 6P5Q), CADD ((PDB ID 1RCW) and FlcD (PDB ID 9B9M). (A) Overall structures. (B) Binding site structures. (C) Sequence alignment.

prepared by adding phosphopantetheinyl-AMP from coenzyme A using the phosphotransferase Sfp.[32] After incubating PPant-bound HamD–T with the truncated adenylation domain of HamD (HamD–A), L-valine, and ATP, a mass increase of 99 Da was observed, corresponding to the addition of valine (*holo*T-Val, Fig. 6C). Further incubation of *holo*T-Val with HamC resulted in mass increase of 16 Da (Fig. 6D) and the resulting product, when reacted with wild-type HamA (wtHamA) and 2OG, showed a molecular weight increase of 32 Da (Fig. 6E), consistent with the formation of HamD–T-Val-hydroxylamine and *holo*T-dihydroxy-valine products. In contrast, the HamA mutants R240A did not exhibit this phenomenon under the same conditions (Fig. 6F). These results indicate that HamA can oxidize HamD–T-Val and that its activity is 2OG-dependent.

Using Foldseek, four heme oxygenase-like domain-containing oxidases are found to be the most structurally similar to HamA (Fig. 7), although they share low sequence homology (Fig. S3).[33] Three of them, SznF, UndA and CADD contain a di-iron active center and catalyze two sequential N-hydroxylations of N_{ω}-methyl-L-arginine (L-NMA) to form *N*-hydroxy intermediates, the oxidative decarboxylation of medium-chain fatty acids (C10–C14) into terminal alkenes (α-alkenes), and utilizes its own tyrosine and lysine as synthons to furnish the carboxylate, carbon backbone, and amine group of pABA in a complex multistep mechanism, respectively.[34–37] FlcD, a dioxygenase that catalyzes the excision of an oxime carbon in the biosynthesis of the copper containing antibiotic fluopsin C, contains a mononuclear iron coordinated with one aspartate and two histidines as HamA.[38] This binding site is conserved among HDOs. The substitution of Glu206 for the His residue that typically coordinates the second iron center in other HDOs, combined with the substrate-induced conformational change in the α3 helix, likely explains the lack of binding at the second iron site.
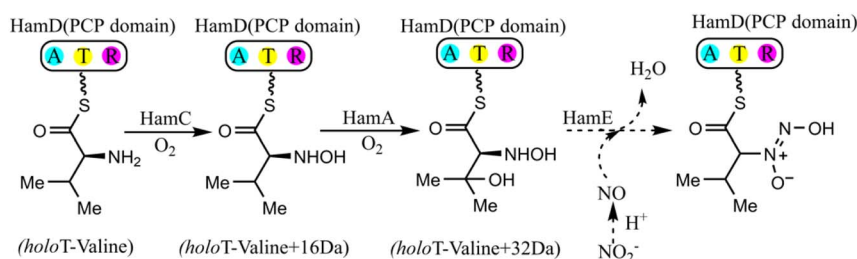

Fig. 8 Proposed mechanism of nitrogen−nitrogen bond formation by HamA, HamC and HamE.

Our research reveals that HamA uniquely binds 2OG, a feature not commonly observed in its homologous proteins, suggesting the evolutionary acquisition of a specialized 2OG-binding site that may support catalytic activity. This capability is consistent with a role in oxidizing *holo*T-valine to a dihydroxy derivative (*holo*T-valine + 32 Da), which could potentially serve as a key intermediate in the proposed biosynthetic pathway of fragin (Fig. 8). Meanwhile, HamC is hypothesized to oxidize amino groups to hydroxylamine groups, implying a possible functional overlap or synergy with HamA in nitrogen–nitrogen (N–N) bond formation. However, the precise division of labor and the potential collaborative mechanism between HamA and HamC remain to be fully elucidated. For example, it is not yet clear whether the hydroxylamine product generated by HamC participates directly in N–N bond formation or requires further oxidation by HamA, nor whether these enzymes operate within a functional complex.

The unique catalytic activities of HamA and HamC suggest promising potential for their application in biocatalysis, particularly in the synthesis of diazeniumdiolate-based compounds, which are of significant pharmaceutical interest due to their diverse bioactivities. The ability of these enzymes to catalyze unusual nitrogen-modifying reactions may enable the efficient production of such molecules under mild and environmentally friendly conditions. Furthermore, the engineering of HamA and HamC—for instance, through directed evolution or structure-based mutagenesis—could facilitate the generation of novel analogs with enhanced antifungal or anticancer properties, offering new avenues for drug development. To fully realize this potential, future studies should focus on elucidating the complete mechanism of N–N bond formation, including structural characterization of possible HamA–HamC functional complexes and detailed *in vivo* metabolic profiling of intermediates. Such efforts would not only deepen our understanding of the enzymology underlying fragin biosynthesis but also provide a foundation for harnessing these enzymes for biotechnological and therapeutic applications.

Conclusions

In summary, our work elucidates HamA, a 2OG-dependent heme-oxygenase-like enzyme featuring a monoiron active center that catalyzes hydroxylation of the product from the nitrogen-oxygenase HamC reaction with *holo*T-valine, providing critical structural insights into the mechanistic formation of the diazeniumdiolate moiety in fragin.

Author contributions

Binbin Su: conceptualization, methodology, investigation, formal analysis, writing-original draft. Tongtong Zhang: data curation, validation, visualization. Yang Yu: resources, supervision, writing-review & editing. Haiping Liu: conceptualization, funding acquisition, supervision, writing – review & editing.

Conflicts of interest

There are no conflicts to declare.

Data availability

The experiment methods and supporting data have been included as part of the supplementary information (SI). Supplementary information is available. See DOI: https://doi.org/10.1039/d5ra05203c.

Acknowledgements

References

1 S. W. Ryter, J. Alam and A. M. Choi, *Physiol. Rev.*, 2006, **86**, 583–650.

2 M. D. Maines and D. Mahin, *Annu. Rev. Pharmacol. Toxicol.*, 1997, **37**, 517–554.

3 M. D. Maines, *FASEB J.*, 1988, **2**, 2557–2568.

4 T. Matsui, M. Furukawa, M. Unno, T. Tomita and M. Ikeda-Saito, *J. Biol. Chem.*, 2005, **280**, 2981.

5 M. Unno, A. Ardèvol, C. Rovira and M. Ikeda-Saito, *J. Biol. Chem.*, 2013, **288**, 34443–34458.

6 S. Adak, N. Ye, L. A. Calderone, M. Duan, W. Lubeck, R. J. B. Schfer, A. L. Lukowski, K. N. Houk, M. E. Pandelia and C. L. Drennan, *Nat. Chem.*, 2024, **16**, 1989–1998.

7 H. Li, J. W. Huang, L. Dai, H. Zheng, S. Dai, Q. Zhang, L. Yao, Y. Yang, Y. Yang, J. Min, R. T. Guo and C.-C. Chen, *Nat. Commun.*, 2023, **14**, 7425.

8 A. V. Toms, A. L. Haas, J. H. Park, T. P. Begley and S. E. Ealick, *Biochemistry*, 2005, **44**, 2319–2329.

9 S. Sieber, C. Daeppen, C. Jenul, V. Mannancherril, L. Eberl and K. Gademann, *Chembiochem*, 2020, **21**, 1587–1592.

10 J. A. Hrabie and L. K. Keefer, *Chem. Rev.*, 2002, **102**, 1135–1154.

11 L. K. Keefer, *ACS Chem. Biol.*, 2011, **6**, 1147–1155.

12 A. M. Kretsch, G. L. Morgan, J. Tyrrell, E. Mevers, I. Vallet-Gely and B. Li, *Org. Lett.*, 2018, **20**, 4791–4795.

13 C. Jenul, S. Sieber, C. Daeppen, A. Mathew, M. Lardi, G. Pessi, D. Hoepfner, M. Neuburger, A. Linden, K. Gademann and L. Eberl, *Nat. Commun.*, 2018, **9**, 1297.

14 G. L. Morgan, A. M. Kretsch, K. C. Santa Maria, S. J. Weeks and B. Li, *Biochemistry*, 2019, **58**, 5249–5254.

15 G. L. Morgan, K. Li, D. M. Crawford, J. Aube and B. Li, *ACS Chem. Biol.*, 2021, **16**, 2776–2786.

16 G. L. Morgan and B. Li, *Angew Chem. Int. Ed. Engl.*, 2020, **59**, 21387–21391.

17 M. Meyer, *Acta Crystallogr., Sect. A:Found. Adv.*, 2015, **71**, 496.

18 R. M. Keegan, A. J. Simpkin and D. J. Rigden, *Acta Crystallogr., Sect. D:Struct. Biol.*, 2024, **80**, 766–779.

19 A. J. Mccoy, A. R. W. Grossekunstleve, B. P. D. Adams, B. M. D. Winn, C. S. A. Laurent and R. J. Randy, *J. Appl. Crystallogr.*, 2007, **40**, 658–674.

20 D. M. Winn, C. C. Ballard, D. K. Cowtan, J. E. Dodson and P. Emsley, *Acta Crystallogr., Sect. D:Biol. Crystallogr.*, 2011, **67**, 235–242.

21 I. Barbarin-Bocahu and M. Graille, *Acta Crystallogr., Sect. D:Struct. Biol.*, 2022, **78**, 517–531.

22 P. Emsley, B. Lohkamp, W. G. Scott and K. Cowtan, *Acta Crystallogr., Sect. D:Biol. Crystallogr.*, 2010, **66**, 486–501.

23 W. L. Delano, *Proteins: Struct., Funct., Bioinf.*, 2002, **30**, 442–454.

24 A. A. Vagin, R. A. Steiner, A. A. Lebedev, L. Potterton and G. N. Murshudov, *Acta Crystallogr.*, 2010, **60**, 2184–2195.

25 R. Huey, G. M. Morris, A. J. Olson and D. S. Goodsell, *J. Comput. Chem.*, 2007, **28**, 1145–1152.

26 Z. Li, H. Wan, Y. Shi and P. Ouyang, *J. Chem. Inf. Comput. Sci.*, 2004, **44**, 1886.

27 M. Asmari, R. Ratih and S. E. Deeb, *Microchem. J.*, 2021, **165**, 106143.

28 A. J. Jasniewski and L. Que Jr, *Chem. Rev.*, 2018, **118**, 2554–2592.

29 L. J. Rajakovich, B. Zhang, M. J. Mcbride, A. K. Boal, C. Krebs and J. M. B. Jr, *Comprehensive Natural Products III*, 3rd edn, 2020, vol. 5, pp. 215–250.

30 E. C. Theil, *Annu. Rev. Biochem.*, 2003, **56**, 289–315.

31 M. B. W. Li, G. Zhao and J. Zhou, *J. Am. Chem. Soc.*, 2023, **145**, 27131–27139.

32 M. M. Nakano, N. Corbell, J. Besson and P. Zuber, *Mol. Gen. Genet.*, 1992, **232**, 313–321.

33 M. V. Kempen, S. Kim, C. Tumescheit, M. Mirdita, J. Soeding and M. Steinegger, *Nat. Biotechnol.*, 2024, **42**, 243–246.

34 M. J. McBride, S. R. Pope, K. Hu, C. D. Okafor, E. P. Balskus, J. M. Bollinger and A. K. Boal, *Proc. Natl. Acad. Sci. U. S. A.*, 2021, **118**, 1–7.

35 R. Schwarzenbacher, F. Stenner-Liewen, H. Liewen, H. Robinson and R. C. Liddington, *J. Biol. Chem.*, 2004, **279**, 29320–29324.

36 B. Zhang, L. J. Rajakovich, D. V. Cura, E. J. Blaesi and J. M. Bollinger, *J. Am. Chem. Soc.*, 2019, **141**, 14510–14514.

37 H. N. Phan, P. D. Swartz, M. Gangopadhyay, Y. Guo, A. I. Smirnov and T. M. Makris, *Biochemistry*, 2024, **63**, 3020–3029.

38 W. C. Simke, M. E. Walker, L. A. Calderone, A. T. Putz, J. B. Patteson, C. N. Vitro, C. F. Zizola, M. R. Redinbo, M. E. Pandelia and T. L. Grove, *ACS Cent. Sci.*, 2024, **10**, 1524–1536.